Unraveling the Role of Co-O-Ni motifs in MOF-derived CoNi-LDH for Enhanced Oxygen Evolution Reaction

Di Li, [a,b] Ruihui Gan,[c] Yongping Zheng,[c] Chang Chen [a,b,*] and Jiawei Wan [a,b,*]

a. State Key Laboratory of Biopharmaceutical Preparation and Delivery, Institute of Process Engineering, Chinese Academy of Sciences, 1 North 2nd Street, Zhongguancun, Haidian District, Beijing 100190, P.R. China.

b. University of Chinese Academy of Sciences, Yuquan Road, Beijing 100049, P. R. China.

c. Advanced Energy Storage Technology Research Center, Shenzhen Institutes of Advanced Technology, Chinese Academy of Sciences Shenzhen 518055, P. R. China.

Experimental Sections

Chemicals and reagents: $Co(NO_3)_2 \cdot 6H_2O$ (98%, Alfa), $Ni(NO_3)_2 \cdot 6H_2O$ (98%, Alfa), 2-methylimidazole (2MI, 99%, Acros), Ethanol (99.8%, AR grade, Beijing Chemical Reagent Factory), sodium dodecyl sulfate (SDS, 98%, Beijing Chemical Reagent Factory), Ultrapure water (Millipore Milli-Q grade) with a resistivity of 18.2 MΩ was used in all the experiments. All of the chemicals used in this experiment were used as received without any further purification.

Synthesis of MDCoNi-LDH：First, 0.8 g SDS was completely dissolved in 100 ml ultrapure water under strongly stirring, followed by adding with 0.708 g $Co(NO_3)_2 \cdot 6H_2O$. Then, 1.598 g of 2-MIm was well dispersed in 10 ml ultrapure water. Next, the solution of 2-MIm was rapidly injected into the mixture solution. After one-hour reaction, the product was collected with centrifugation and washed with deionized water and ethanol for three times, respectively. At this point, the ZIF 67 nanoplates sample was successfully synthesized. After that, the powder was fully dispersed into 50 ml ethanol and then added with 0.177 g $Ni(NO_3)_2 \cdot 6H_2O$. After reaction for half one-hour, the product was collected with centrifugation and washed with deionized water and ethanol for three times, respectively. The MDCoNi-LDH powder was collected by freeze-drying method.

Synthesis of $Co(OH)_2$：First, 0.8 g SDS was completely dissolved in 100 ml ultrapure water under strongly stirring, followed by adding with 0.708 g $Co(NO_3)_2 \cdot 6H_2O$. Then, 1.598 g of 2-MIm was well dispersed in 10 ml ultrapure water. Next, the solution of 2-MIm was rapidly injected into the mixture solution. After one-hour reaction, the

product was collected with centrifugation and washed with deionized water and ethanol for three times, respectively. After that, the powder was fully dispersed into 50 ml ethanol and then added with 0.177 g $Co(NO_3)_2 \cdot 6H_2O$. After reaction for half one-hour, the product was collected with centrifugation and washed with deionized water and ethanol for three times, respectively. The sample was subjected to freeze-drying in a lyophilizer for 12 h to obtain the final product $Co(OH)_2$.

Characterization

Transmission electron microscopy (TEM) analysis was performed by JEM 2100F at 200 kV. Surface morphology was observed on a field emission scanning electron microscope (SU8020, Hitachi). X-ray diffraction (XRD) data were collected by an SmartLab (Rigaku SmartLab 9 kW), equipped with Cu Kα radiation (λ= 0.15406nm). Inductively Coupled Plasma-Optical Emission Spectrometer (IP-OES, Avio 220 MAX). X-ray photoelectron spectroscopy (XPS) measurements were carried out by XPS spectrometer (ESCALAB 250Xi, Thermo Fisher Scientific). The binding energies of the XPS analysis were standardized against the C 1s line (284.8 eV). Electrochemical performance was performed with a CHI 760E electrochemical workstation (CHI instruments) systems equipped with a standard three-electrode cell.

Electrochemical measurements

The electrochemical measurements were performed in a three-electrode system with a CHI760E electrochemical workstation (Shanghai, ChenHua Instrument Co., Ltd.). All the materials were cut into 1 cm × 1 cm and used as directly. The Hg/HgO and graphite rods were used as the reference electrode and the counter electrode, respectively. If not

otherwise specified, the electrolyte utilized in the experiments was consistently maintained in 1.0 M KOH. Polarization curves were obtained through linear sweep voltammetry testing (LSV), with a scan rate of 1 mV^{-1}. The stability of the catalyst is evaluated using the chronopotentiometry method. All the potentials were converted to the reversible (RHE) using the equation:

$$E(vs\ RHE) = E(Hg/HgO) + 0.0592 * pH + 0.098$$

Electrostatic double-layer capacitor (C_{dl}) was measured by cyclic voltammetry cyclic voltammetry (CVs) at multiple scan rates (10, 20, 40, 60, 80, 100 $mV \cdot s^{-1}$) over a voltage range of 0.176 to 0.276 V vs. Hg/HgO. C_{dl} is calculated as the linear slope of half the difference in current density at the anode and cathode relative ($\Delta j = (|j_{charge} - j_{discharge}|/ 2)$ to the scan rate. Electrochemically active surface areas (ECSAs) were calculated according to the formula:

$$ECSA = \frac{C_{dl}}{C_s}$$

C_s is the specific capacitance of the standard electrode.

TOF were calculated according to the following equation :

$$TOF = \frac{j \times A}{n \times F \times m}$$

where j is the current density at a certain potential, A represents the geometrical area of the working electrode (1 cm^2), m denotes the number of electrons transferred during the generation of an O_2 molecule, F is the Faraday constant (96485 C/mol), and n is the total metal ion moles.

Calculation details

Spin-polarized density functional theory (DFT) calculations were performed using the

Vienna Ab initio Simulation Package (VASP, version 6.4.0). [1,2] The electron-ion interactions were described by the projector augmented wave (PAW) method. [3] The exchange-correlation functional was treated within the generalized gradient approximation (GGA) using the Perdew-Burke-Ernzerhof (PBE) formulation. [4] To account for the on-site Coulomb interactions of the localized 3*d* electrons of Co and Ni atoms, the GGA+U approach was employed with the Dudarev implementation, where an effective Hubbard parameter $U_{\text{eff}} = U - J$ (with $J = 0$ eV) = 3.0 eV for Co and 6.0 eV for Ni and was applied.

A plane-wave kinetic energy cutoff of 450 eV was used. The Brillouin zone was sampled with a Monkhorst-Pack k-point grid of 2×2×1 for structural relaxation. The electronic self-consistent loop was converged to 10^{-4} eV, and the geometries were optimized until the residual forces on all unrestricted atoms were less than 0.02 eV/Å. A vacuum layer of at least 15 Å was added in the z-direction of the constructed CoOOH and CoNiOOH models to separate periodic images.

The oxygen evolution reaction (OER) catalytic activity for CoOOH and CoNiOOH was evaluated by calculating the Gibbs free energy change (ΔG) for each elementary step (*OH, *O, and *OOH). The adsorption Gibbs free energy of adsorptions (ΔG_{ads}) was calculated according to the equation:

$$\Delta G_{\text{ads}} = \Delta E_{\text{ads}} + \Delta E_{\text{ZPE}} - T\Delta S$$

Here, ΔE_{ads} is the adsorption energy obtained directly from DFT total energies, and T is temperature. ΔE_{ZPE} and ΔS are the differences in zero-point energy and entropy between the adsorbed state and the corresponding free molecules in the gas phase.

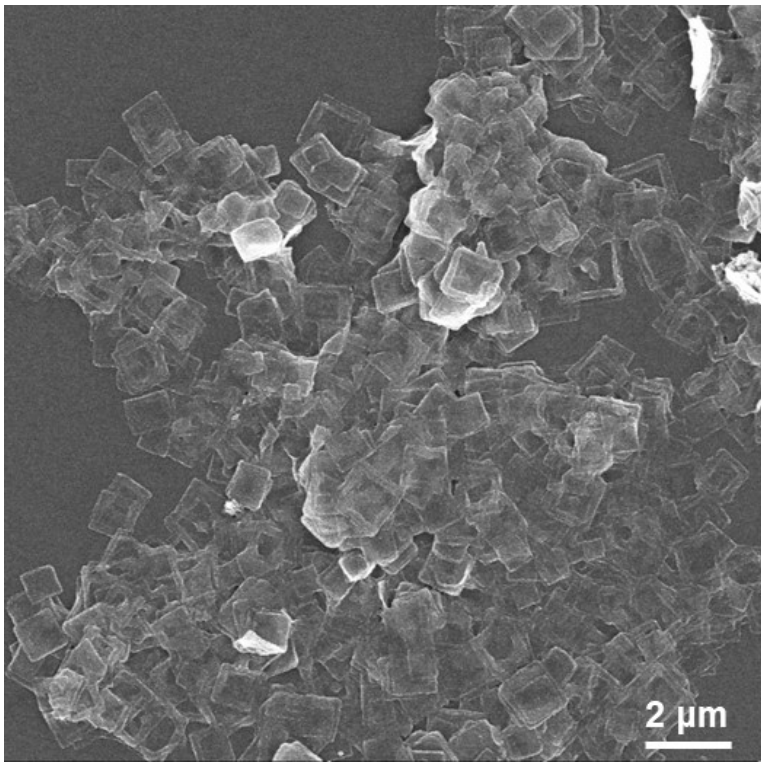

Fig. S1. SEM image of ZIF 67-nanoplates

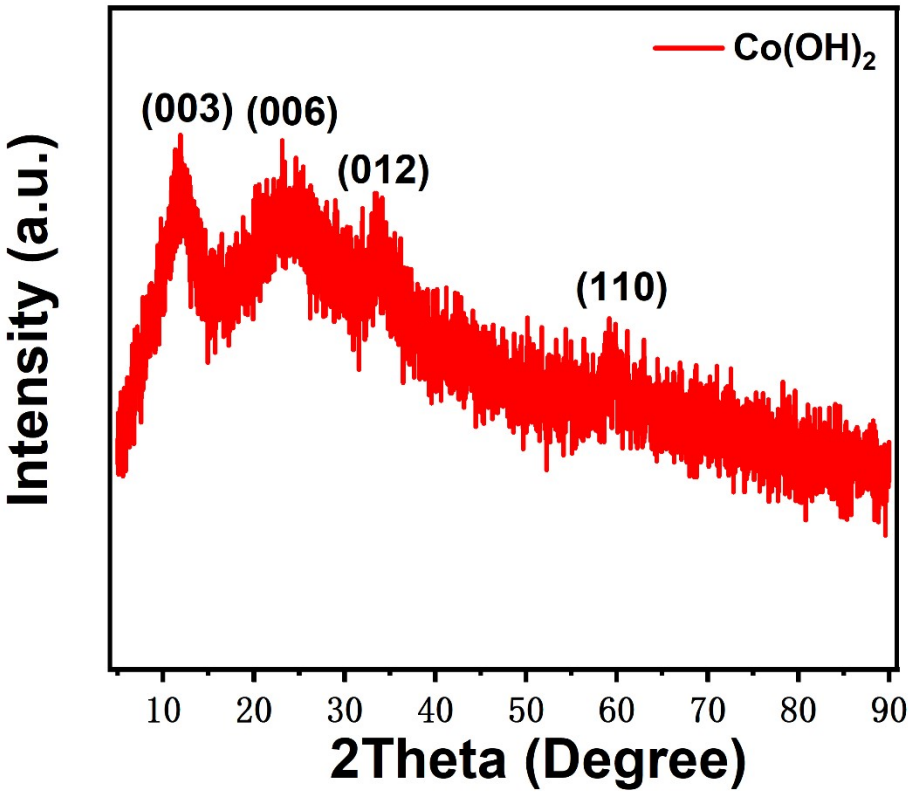

Fig. S2. XRD patterns of $Co(OH)_2$.

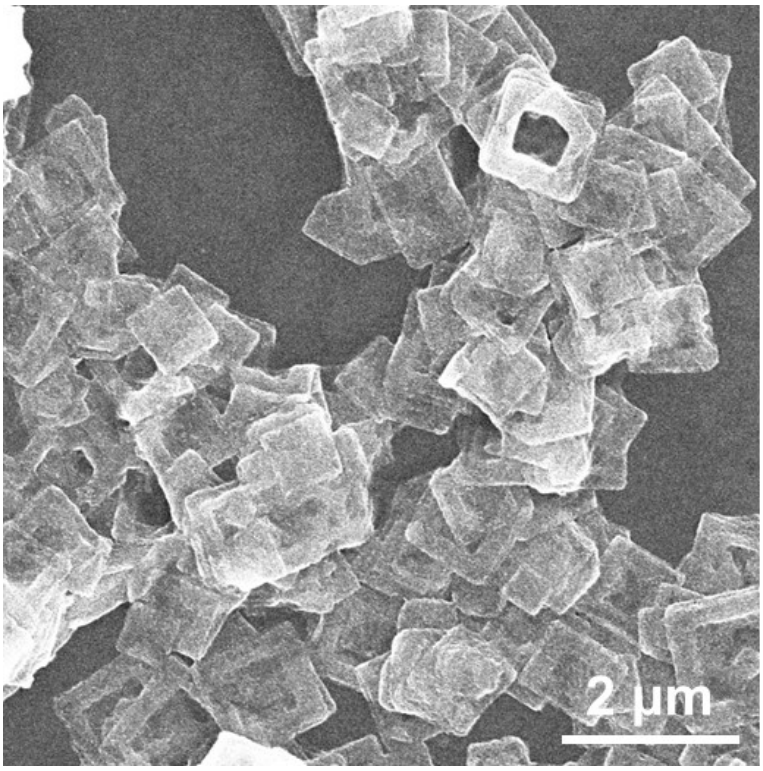

Fig. S3. SEM image of MDCoNi-LDH.

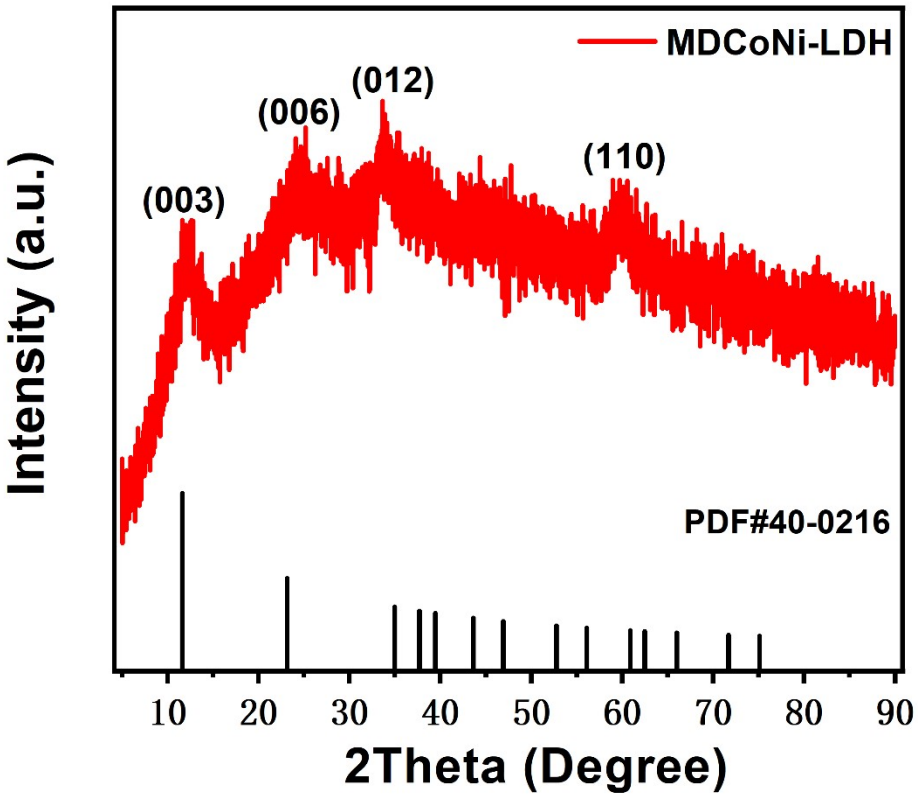

Fig. S4. XRD patterns of MDCoNi-LDH.

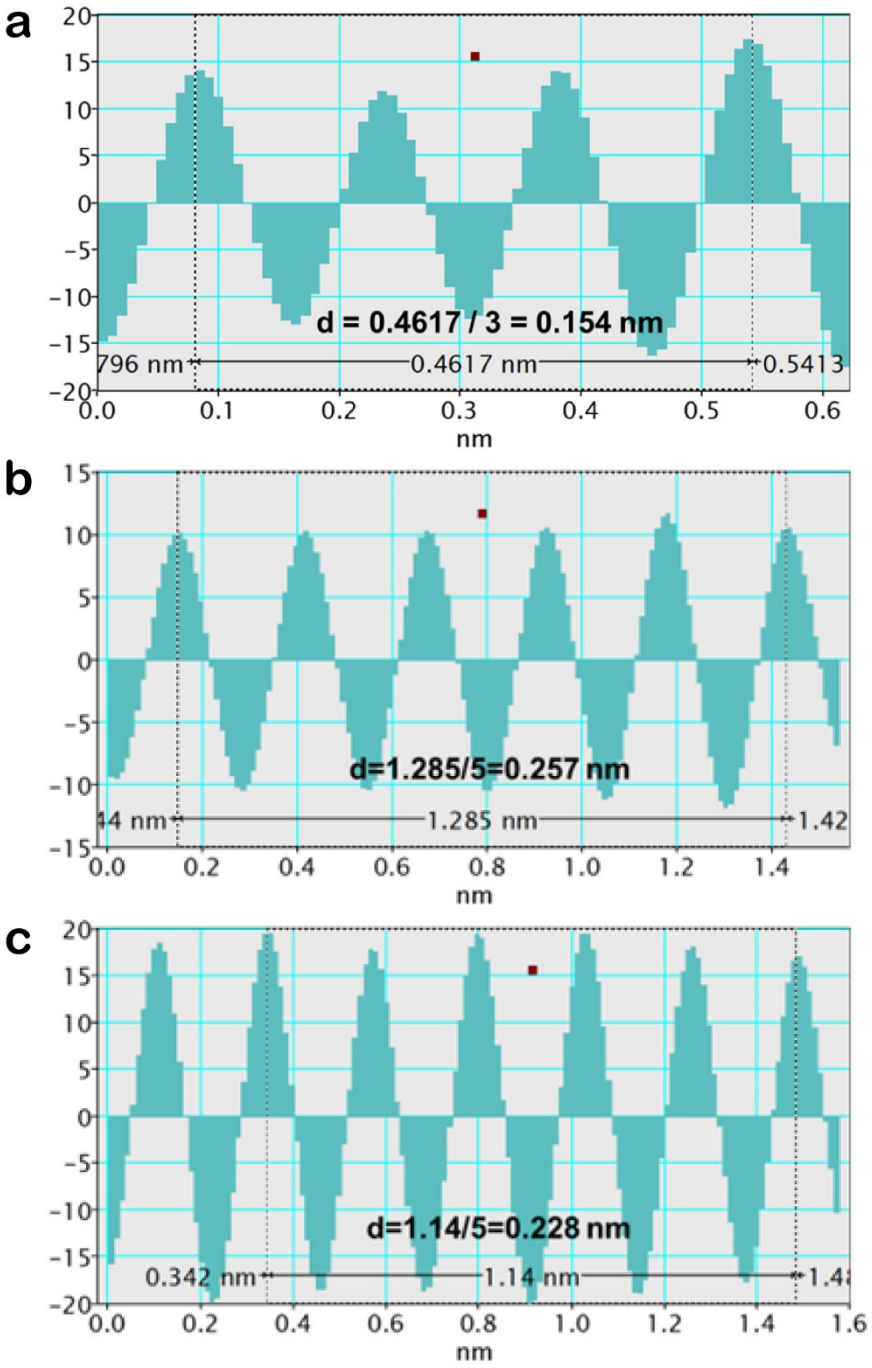

Fig. S5. Profile of inverse FFT with d-spacing distance for MDCoNi-LDH with different facets such as (a) (110), (b) (012), (c) (015).

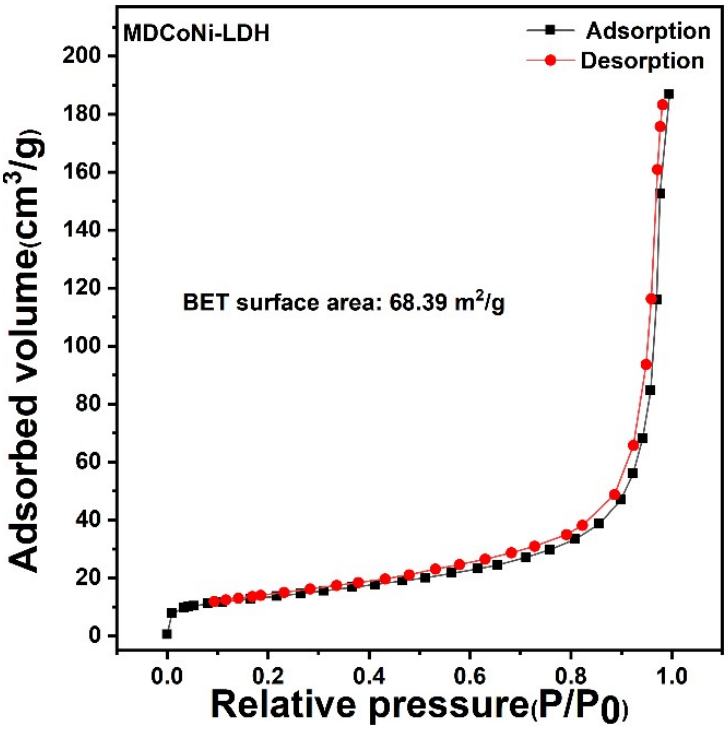

Fig. S6. Nitrogen adsorption–desorption isotherms of MDCoNi-LDH catalyst.

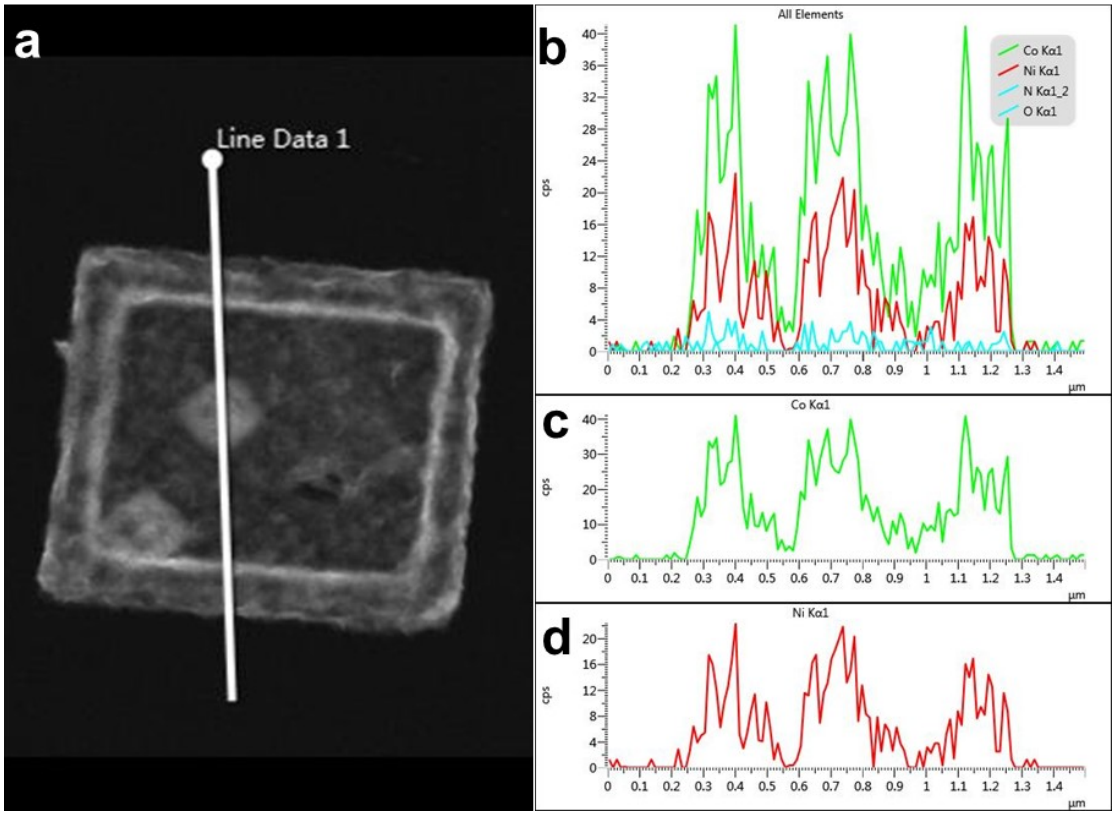

Fig. S7. Line scan of energy dispersive X-ray spectroscopy (EDX) for MDCoNi-LDH

(a) HAADF, (b) all elements, (c) Co, (d) Ni.

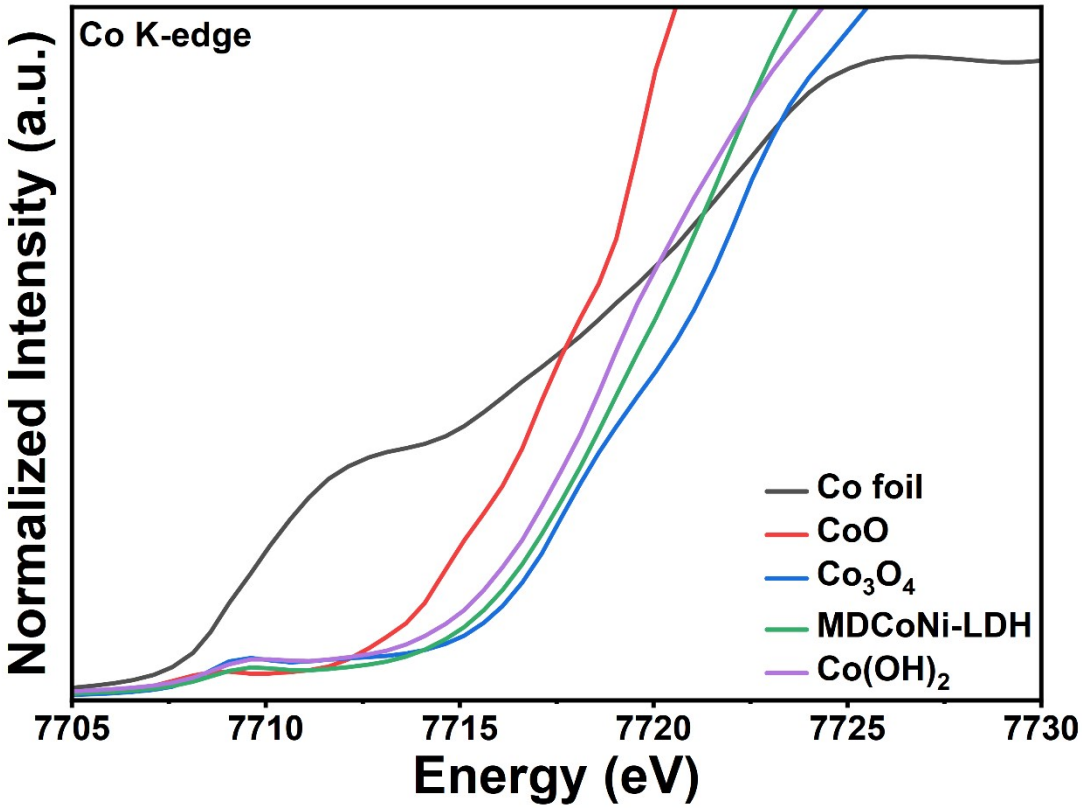

Fig. S8. X-ray absorption near-edge structure (XANES) spectra of Co K-edge in different magnification.

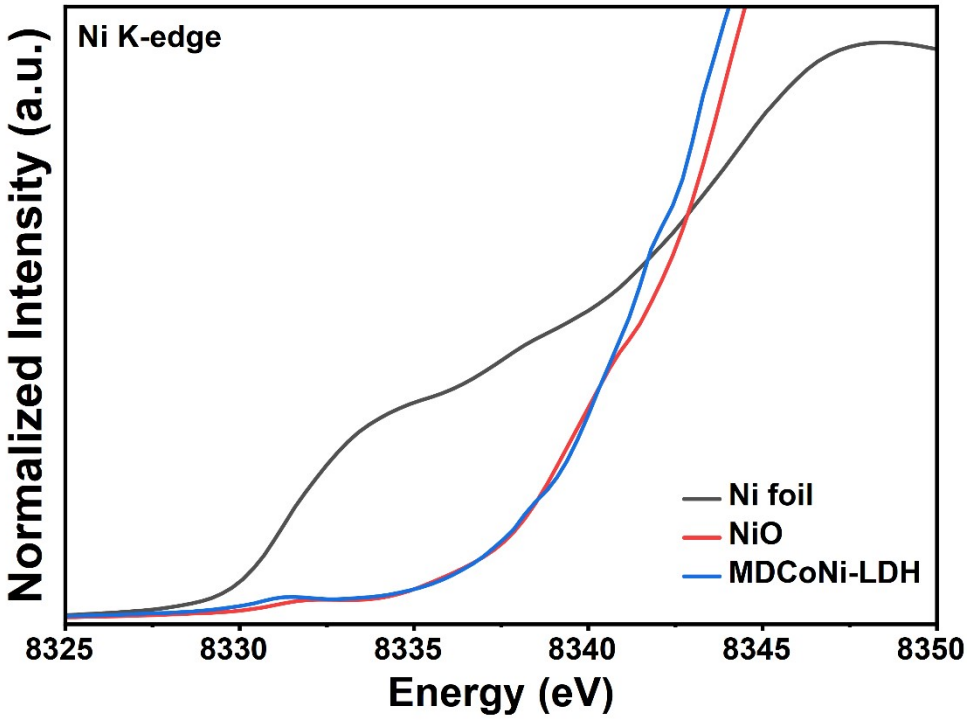

Fig. S9. XANFS spectra of Ni K-edge in different magnification.

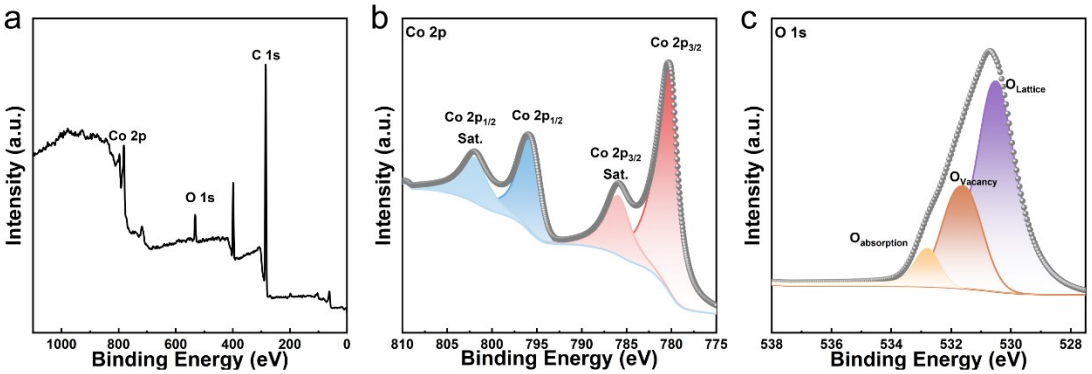

Fig. S10. XPS spectra of $Co(OH)_2$ (a) survey, (b) Co 2p and (c) O 1s.

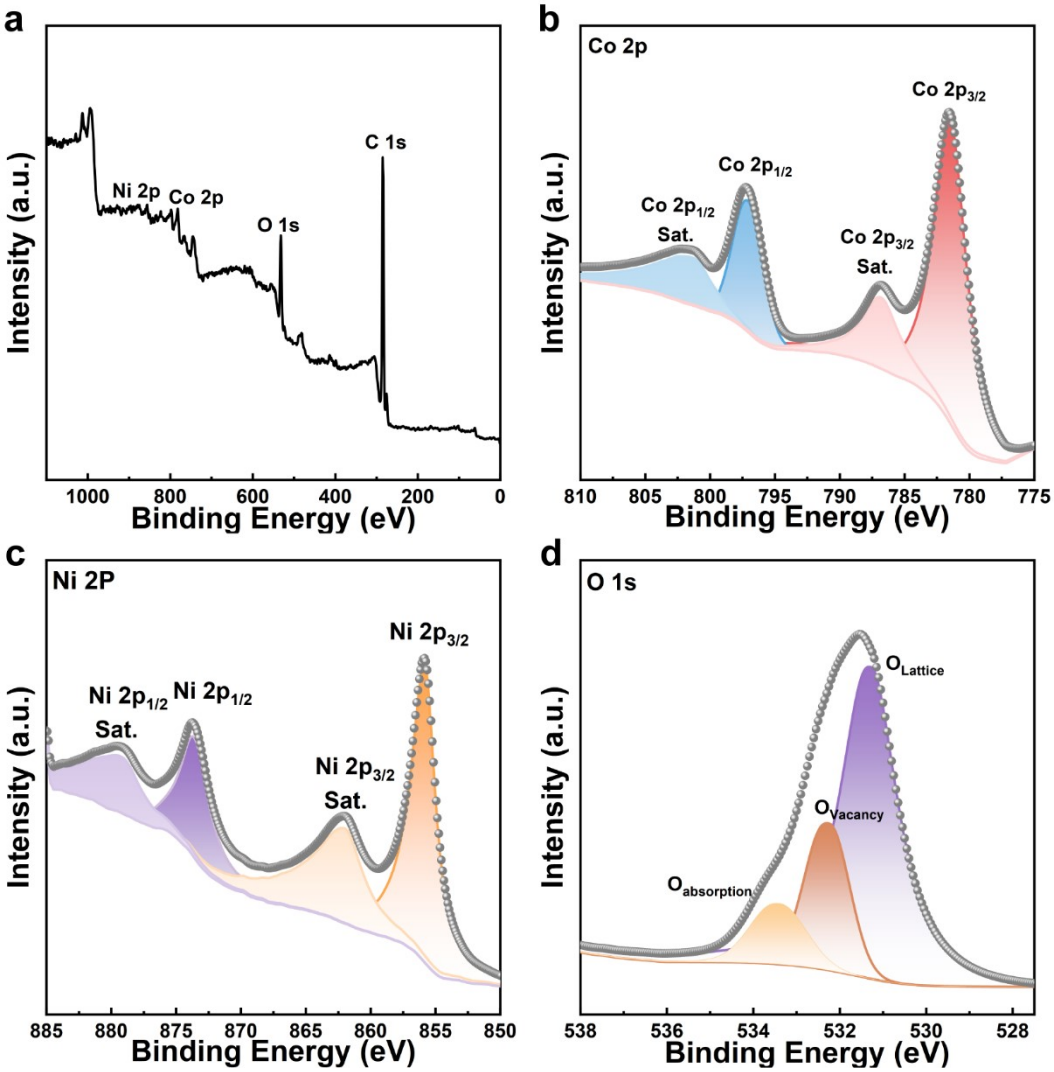

Fig. S11. XPS spectra of MDCoNi-LDH (a) survey, (b) Co 2p, (c)Ni 2p and (d) O 1s.

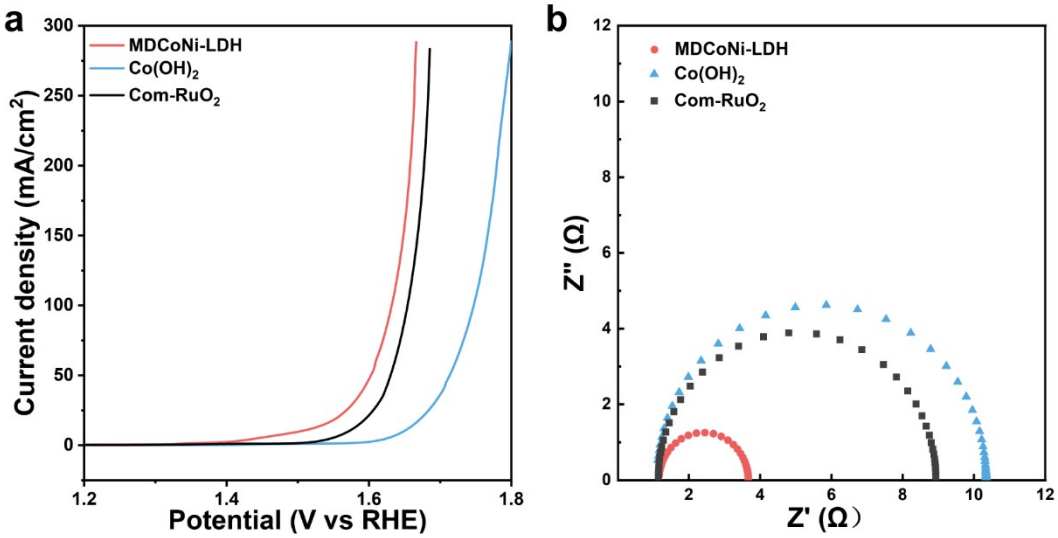

Fig. S12. LSV curves with 90% *iR* compensation (a) and EIS Nyquist plots (b) of MDCoNi-LDH, $Co(OH)_2$ and commercial RuO_2.

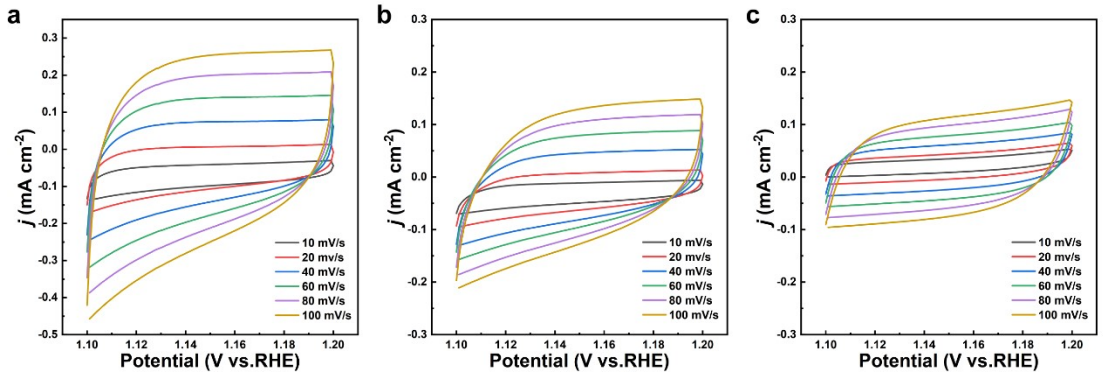

Fig. S13. CV curves of (a) MDCoNi-LDH, (b) commercial RuO_2 and (c) $Co(OH)_2$ in a non-Faradaic region at scan rates of 10, 20, 40, 60, 80, and 100 $mV \cdot s^{-1}$ for OER.

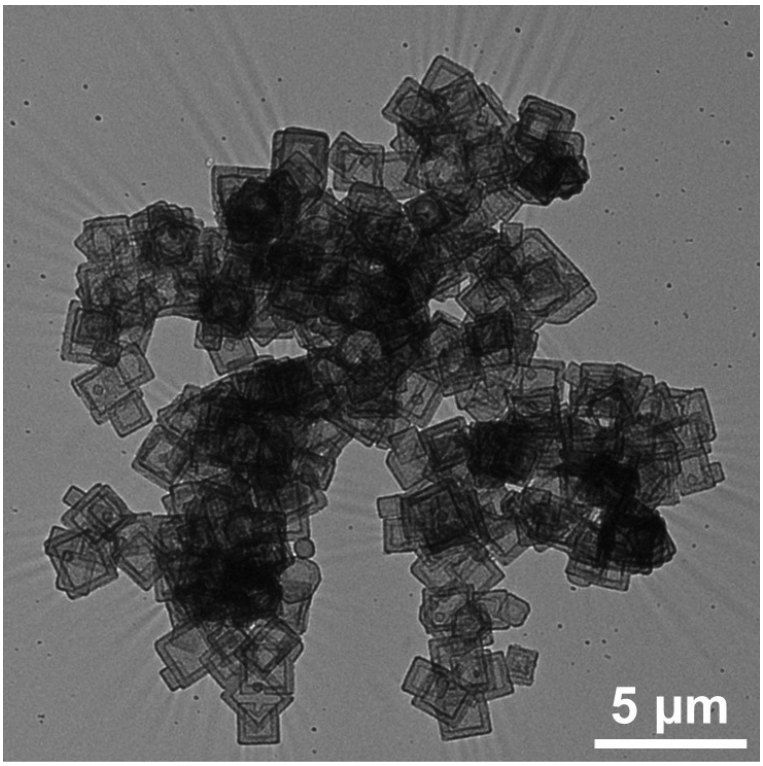

Fig. S14. TEM image of MDCoNi-LDH after OER test.

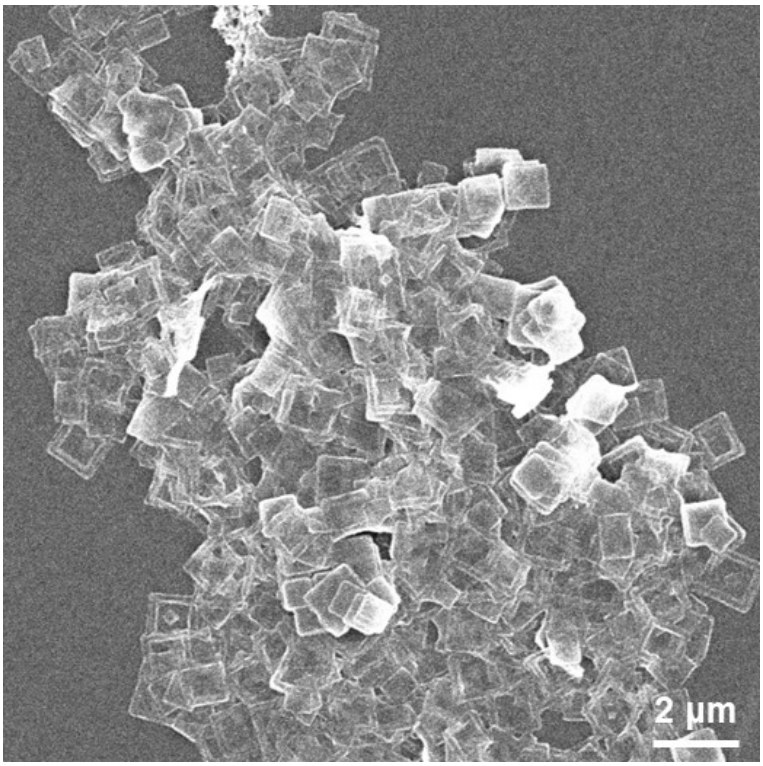

Fig. S15. SEM image of MDCoNi-LDH after OER test.

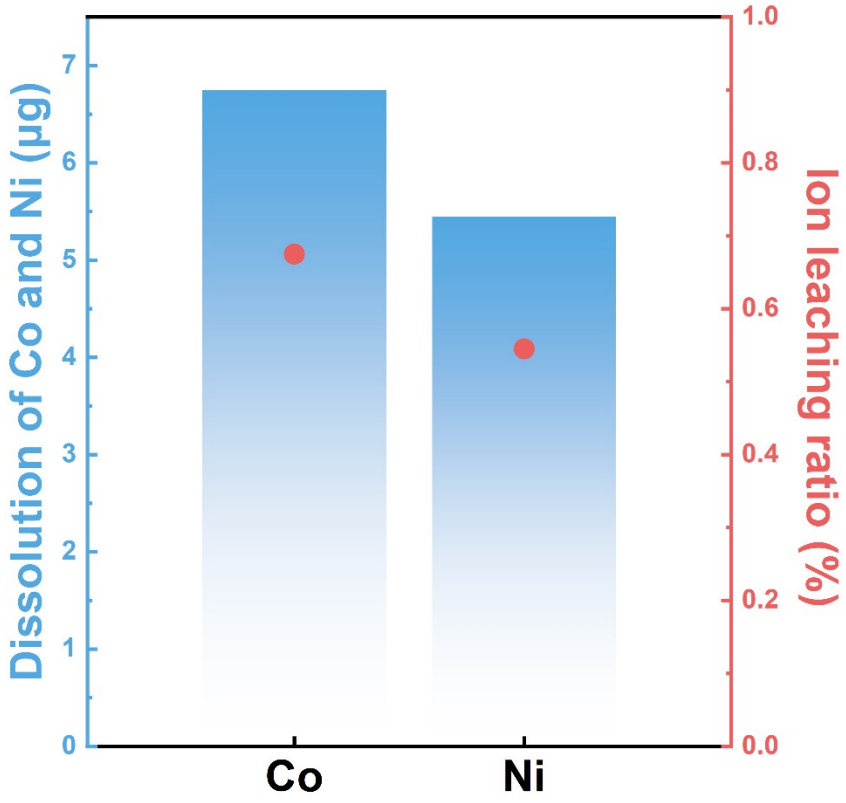

Fig. S16. Leaching mass and ion leaching ratio of Co and Ni of MDCoNi-LDH after 140h of OER.

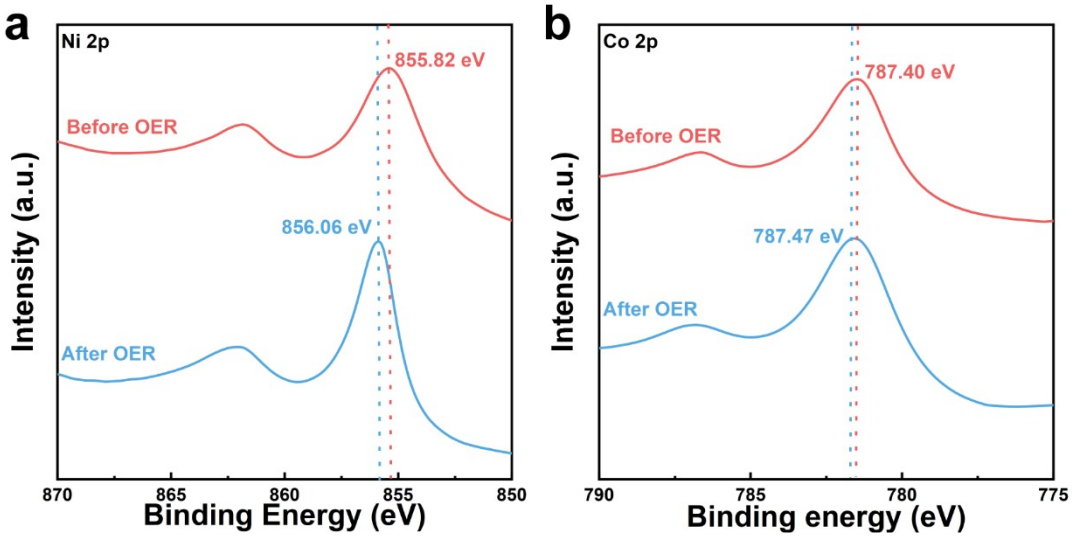

Fig. S17. XPS of MDCoNi-LDH before and after OER process.

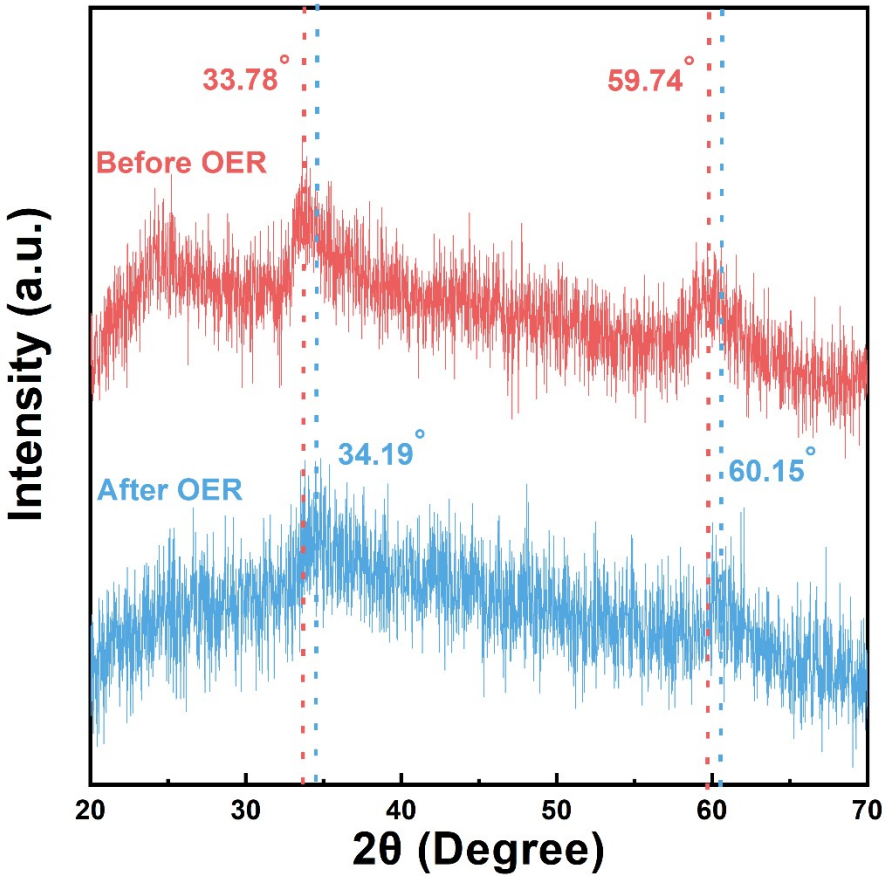

Fig. S18. XRD patterns of MDCoNi-LDH before and after OER process.

Table S1. The EXAFS fitting result of Co K-edge. (S_0^2 = 0.84)

Sample	Path	CN	R(Å)	σ^2(10^{-3}Å^2)	ΔE_0(eV)	R factor
MDCoNi-LDH	Co-O	4.4±0.88	2.02±0.02	3.5±0.70	2.6±0.52	0.009
	Co-Ni/Co	4.9±0.98	3.14±0.03	4.2±0.84	3.4±0.68	
$Co(OH)_2$	Co-O	4.0±0.8	2.01±0.02	3.7±0.74	2.8±0.56	0.012
	Co-Co	5.1±1.02	3.16±0.03	4.7±0.94	3.5±0.70	

S_0^2 is the amplitude reduction factor; CN is the coordination number; R is interatomic distance (the bond length between Ru central atoms and surrounding coordination atoms); σ^2 is Debye-Waller factor (a measure of thermal and static disorder in absorber-scatterer distances); ΔE_0 is edge-energy shift (the difference between the zero kinetic energy value of the sample and that of the theoretical model). R factor is used to value the goodness of the fitting.

* This value was fixed during EXAFS fitting, based on the known structure.

Error bounds that characterize the structural parameters obtained by EXAFS spectroscopy were estimated as CN ± 20%; R ± 1%; σ^2 ± 20%; ΔE_0 ± 20%.

Table S2. The EXAFS fitting result of Ni K-edge. (S_0^2 = 0.82)

Sample	Path	CN	R(Å)	$\sigma^2(10^{-3}Å^2)$	ΔE_0(eV)	R factor
MDCoNi-LDH	Ni-O	5.2±1.04	1.99±0.02	4.2±0.84	3.1±0.64	0.013
	Ni-Co/Ni	4.8±0.96	3.12±0.03	4.8±0.96	3.8±0.76	

S_0^2 is the amplitude reduction factor; CN is the coordination number; R is interatomic distance (the bond length between Ru central atoms and surrounding coordination atoms); σ^2 is Debye-Waller factor (a measure of thermal and static disorder in absorber-scatterer distances); ΔE_0 is edge-energy shift (the difference between the zero kinetic energy value of the sample and that of the theoretical model). R factor is used to value the goodness of the fitting.

* This value was fixed during EXAFS fitting, based on the known structure.

Error bounds that characterize the structural parameters obtained by EXAFS spectroscopy were estimated as CN ± 20%; R ± 1%; σ^2 ± 20%; ΔE_0 ± 20%.

Table S3. OER performance comparison of Catalysts

Catalyst	Overpotential (mV,10mA cm^{-2})	Tafel slope (mV/dec)	Stability (h)	TOF (s^{-1})	References
NiFe-PBA/CoV-LDH	300	79.21	8	10.54 × 10^{-5}	5
NiFe-LDH-PTA	349 for 1000 mA cm^{-2}	83.28	500	0.136	6
$Co_{2.8}W_{3.8}$-NiFe LDH	255 for 1000 mA cm^{-2}	37.8	200	4.02	7
$NaBH_4$–NiFe LDHs	280	58.7	6.67	-	8
Fe-Co LDH/MoP	240	39.6	36	-	9
NiCoFe-LDH	300	112	8	-	10
NiCo–CH	343	66	2.5	-	11
NiCo-LDH-OH	317	92.10	20	-	12
NiFe-LDH/3D GA	257	46.6	56	-	13
NiFe-LDH/MoCN	323	132.9	12	-	14
$Co_3[Co(CN)_6]_2$ @NiFe LDH	253	54	10	-	15
Ni-BDC/LDH	218	108	72	-	16
Cu/NiFe LDH	259	36.53	12	-	17
NiFe LDH	290	87.84	11	-	18
MDCoNi-LDH	278	90.93	140	0.026	This work

Table S4. The Gibbs free energies of OER with DFT calculations for catalysts of CoNiOOH

		Total	Gibbs
slab	-540.88	-583.7	0
*OH	-550.27	-582.385	1.315
*O	-545.19	-580.82	2.88
*OOH	-555.1	-580.025	3.675
O_2+2H_2O	-540.88	-578.79	4.91

Table S5. The Gibbs free energies of OER with DFT calculations for cataalysts of CoOOH

		Total	Gibbs
slab	-555.59	-598.41	0
*OH	-564.7	-596.815	1.595
*O	-560.13	-595.76	2.65
*OOH	-569.68	-594.605	3.805
O_2+2H_2O	-555.59	-593.5	4.91

Reference

1. Kresse, G.; Hafner, J. Ab Initio Molecular Dynamics for OpenShell Transition Metals. Phys. Rev. B 1993, 48 (17), 13115−13118.
2. Kresse, G.; Hafner, J. Ab Initio Molecular Dynamics for Liquid Metals. Phys. Rev. B 1993, 47 (1), 558−561.
3. Kresse, G.; Joubert, D. From Ultrasoft Pseudopotentials to the Projector Augmented-Wave Method. Phys. Rev. B 1999, 59 (3), 1758−1775.
4. Perdew, J. P.; Burke, K.; Ernzerhof, M. Generalized Gradient Approximation Made Simple. Phys. Rev. Lett. 1996, 77 (18), 3865−3868.
5. V. Singh, S. Singh, A. Tiwari, S. Dubey, S. Pandey, A. Yadav, R. Bhatia and V. Ganesan, *Electrochim. Acta*, 2026, **547,** 147828.
6. J. Zhang, X. Zhang, Z. Ma, K. Fang, L. Wang, H. Ni and B. Zhao, *ACS Catal.,* 2025, 15, 8, 6486–6496.
7. Y. Shi, L. Song, Y. Liu, T. Wang, C. Li, J. Lai and L. Wang. *Adv. Energy Mater.* 2024, 14, 2402046.
8. Y. Wang, S. Tao, H. Lin, S. Han, W. Zhong, Y. Xie, J. Hu and S. Yang, *RSC Adv*., 2020, **10**, 33475–33482.
9. G. An, C. Zhou, C. Wu, B. Gao, S. Xu and Q. Xu, *Small*, 2025, ee05953.
10. V. Poormirzaei and Z. Rezvani, *Chem. Select*, 2023, **8**, e202301941.
11. S. Wang, T. Wang, X. Wang, Q. Deng, J. Yang, Y. Mao and G. Wang, *Int. J. Hydrog. Energy*, 2020, **45**, 12629–12640.
12. H. Yang, Z. Zhou, H. Yu, H. Wen, R. Yang, S. Peng, M. Sun and L. Yu, *J. Colloid Interface Sci.*, 2023, **636**, 11–20.
13. J. Zhang, Q. Cao, X. Yu, H. Yao, B. Su and X. Guo, *Nanomaterials*, 2024, **14**, 1611.
14. Y. Du, Y. Zhang, X. Pu, X. Fu, X. Li, L. Bai, Y. Chen and J. Qian, *Chemosphere*, 2023, **312**, 137203
15. J. Yu, R. Fu, S. Ge, C. Yang, Y. Zhao, C. Feng, Q. Jiao and H. Li, *New J. Chem*, 2024, **48**, 6625–6632.
16. D. Li, X. Guo, Z. Xu, Q. Chen, R. Liu and C. Li, *Chem. Select*, 2025, **10**, e202404610.
17. F. Du, J. Yao, H. Luo, Y. Chen, Y. Qin, Y. Du, Y. Wang, W. Hou, M. Shuai and C. Guo, *Green Chem.*, 2024, **26**, 895–903.
18. D. Li, M. Mushtaq, Y. Tang, S. Li, F. Hou, K. Ayub, L. Cao and J. Yang, *Res. Chem. Intermed.*, 2025, **51**, 3019–3038.